

Electronic transitions and dielectric functions of relaxor ferroelectric $\text{Pb}(\text{In}_{1/2}\text{Nb}_{1/2})\text{O}_3\text{-Pb}(\text{Mg}_{1/3}\text{Nb}_{2/3})\text{O}_3\text{-PbTiO}_3$ single crystals: Temperature dependent spectroscopic study

J. J. Zhu, J. Z. Zhang, G. S. Xu, X. L. Zhang, Z. G. Hu, and J. H. Chu

Citation: *Applied Physics Letters* **104**, 132903 (2014); doi: 10.1063/1.4870426

View online: <http://dx.doi.org/10.1063/1.4870426>

View Table of Contents: <http://scitation.aip.org/content/aip/journal/apl/104/13?ver=pdfcov>

Published by the *AIP Publishing*

Articles you may be interested in

[Broadband inelastic light scattering study on relaxor ferroelectric \$\text{Pb}\(\text{In}_{1/2}\text{Nb}_{1/2}\)\text{-Pb}\(\text{Mg}_{1/3}\text{Nb}_{2/3}\)\text{O}_3\text{-PbTiO}_3\$ single crystals](#)

J. Appl. Phys. **115**, 234103 (2014); 10.1063/1.4878855

[Electrocaloric properties in relaxor ferroelectric \$\(1-x\)\text{Pb}\(\text{Mg}_{1/3}\text{Nb}_{2/3}\)\text{O}_3\text{-xPbTiO}_3\$ system](#)

J. Appl. Phys. **114**, 174105 (2013); 10.1063/1.4829012

[Temperature-dependent Raman scattering and multiple phase coexistence in relaxor ferroelectric \$\text{Pb}\(\text{In}_{1/2}\text{Nb}_{1/2}\)\text{O}_3\text{-Pb}\(\text{Mg}_{1/3}\text{Nb}_{2/3}\)\text{O}_3\text{-PbTiO}_3\$ single crystals](#)

J. Appl. Phys. **114**, 153508 (2013); 10.1063/1.4825322

[Temperature-dependent dielectric functions and interband critical points of relaxor lead hafnate-modified \$\text{PbSc}_{1/2}\text{Ta}_{1/2}\text{O}_3\$ ferroelectric ceramics by spectroscopic ellipsometry](#)

Appl. Phys. Lett. **102**, 151908 (2013); 10.1063/1.4802205

[Phase transition behaviors in relaxor ferroelectric \$\[001\]\$ -poled \$\text{Pb}\(\text{In}_{1/2}\text{Nb}_{1/2}\)\text{O}_3\text{-Pb}\(\text{Mg}_{1/3}\text{Nb}_{2/3}\)\text{O}_3\text{-PbTiO}_3\$ single crystals studied by Brillouin light scattering and dielectric spectroscopies](#)

J. Appl. Phys. **111**, 054103 (2012); 10.1063/1.3692596

An advertisement for Asylum Research Cypher AFMs. The background is dark blue with a film strip graphic on the left. The text is in white and orange. The Oxford Instruments logo is in the bottom right corner.

Not all AFMs are created equal
Asylum Research Cypher™ AFMs
There's no other AFM like Cypher

www.AsylumResearch.com/NoOtherAFMLikeIt

OXFORD
INSTRUMENTS
The Business of Science®

Electronic transitions and dielectric functions of relaxor ferroelectric $\text{Pb}(\text{In}_{1/2}\text{Nb}_{1/2})\text{O}_3\text{-Pb}(\text{Mg}_{1/3}\text{Nb}_{2/3})\text{O}_3\text{-PbTiO}_3$ single crystals: Temperature dependent spectroscopic study

J. J. Zhu (诸佳俊),^{1,2} J. Z. Zhang (张金中),^{1,2} G. S. Xu (许桂生),³ X. L. Zhang (张小龙),¹ Z. G. Hu (胡志高),^{1,a)} and J. H. Chu (褚君浩)^{1,2}

¹Key Laboratory of Polar Materials and Devices, Ministry of Education, Department of Electronic Engineering, East China Normal University, Shanghai 200241, China

²National Laboratory for Infrared Physics, Shanghai Institute of Technical Physics, Chinese Academy of Sciences, Shanghai 200083, China

³R&D Center of Synthetic Crystals, Shanghai Institute of Ceramics, Chinese Academy of Sciences, Shanghai 201800, China

(Received 6 February 2014; accepted 23 March 2014; published online 1 April 2014)

Optical properties and phase transitions of $\text{Pb}(\text{In}_{1/2}\text{Nb}_{1/2})\text{O}_3\text{-Pb}(\text{Mg}_{1/3}\text{Nb}_{2/3})\text{O}_3\text{-PbTiO}_3$ (PIN-PMN-PT) crystals near morphotropic phase boundary (MPB) have been investigated by temperature dependent transmittance and reflectance spectra. Three critical point energies $E_g = 3.17\text{--}3.18$ eV, $E_a = 3.41\text{--}3.61$ eV, and $E_b = 4.74\text{--}4.81$ eV can be assigned to the transitions from oxygen $2p$ to titanium d , niobium d , and lead $6p$ states, respectively. They show narrowing trends with increasing temperature, which can be caused by thermal expansion of the lattice and electron-phonon interaction. Deviation from the linear behaviors can be observed from E_a and E_b versus PT concentration, indicating a complex multiphase structure near MPB region. © 2014 AIP Publishing LLC. [<http://dx.doi.org/10.1063/1.4870426>]

Relaxor ferroelectrics with peculiar characteristics of ferroelectricity and piezoelectricity can be used in the fields for sensors, nonvolatile random access memories, electro-optic modulators, pyroelectric detectors, and micro-electromechanical systems.^{1–6} Ferroelectricity in lead (Pb)-based relaxors with ABO_3 perovskite structure is driven mainly by the stereochemical activity of Pb. Nevertheless, the B-site ions primarily affect morphotropic phase boundary (MPB) and facile polarization rotation, providing the disorder and leading to relaxor ferroelectricity.^{2,3} Ionic size effects, A-site-oxygen (O) and B-site-O hybridizations play an important role in competing structural and polar instabilities of perovskites, indicating the complexity of physical mechanism.⁴ The solid solutions of $\text{PbMg}_{1/3}\text{Nb}_{2/3}\text{O}_3\text{-PbTiO}_3$ (PMN-PT) crystallize in a complex ABO_3 perovskite structure, where B-site ions occupy the same crystallographic site in the structure with a complex energy distribution. It has a higher piezoelectric response than that of conventional piezoelectric $\text{PbZr}_x\text{Ti}_{1-x}\text{O}_3$ (PZT) ceramics, especially near the MPB region. Note that a transition occurs from the rhombohedral (R) to tetragonal (T) phase when PT concentration is close to 0.33.⁵ In spite of the recent progress on the development of the PMN-PT crystals, they have a relatively low coercive field ($E_c = 2\text{--}3$ kV/cm) and depoling temperature ($T_{R-T} \approx 80\text{--}90^\circ\text{C}$) due to a strongly curved MPB.⁶ Moreover, large deviations of the refractive index from a linear behavior were observed in PMN below the Burns temperature due to the formation of static or slowly moving polar nano-regions.⁷ This decreases the thermal stability of dielectric and piezoelectric properties and reduces the operation temperature range of the devices, which becomes a critical limitation for applications.

Fortunately, it was found that $\text{Pb}(\text{In}_{1/2}\text{Nb}_{1/2})\text{O}_3\text{-Pb}(\text{Mg}_{1/3}\text{Nb}_{2/3})\text{O}_3\text{-PbTiO}_3$ (PIN-PMN-PT) systems offer a larger coercive field ($E_c \geq 5$ kV/cm) and higher degree of structural instabilities ($T_{R-T} \geq 135^\circ\text{C}$), while the piezoelectric performance is comparable to that of PMN-PT systems. Moreover, temperature dependence of dielectric and piezoelectric properties is more stable, which makes PIN-PMN-PT ternary systems the most promising materials for future device applications. Recently, we reported bandgap narrowing and widening trends with increasing temperature for PIN-PMN-PT crystals near MPB below room temperature (RT).⁸ However, the dielectric functions and electronic band structures at high temperatures have not been fully clarified. Generally, transmittance spectra can provide optical bandgap (OBG), dielectric functions, absorption characteristics, and band tail state behavior by comparing the reasonable dispersion model to experimental spectra. Similarly, spectral reflectance technique can be used to investigate the electronic band energy above the OBG, which cannot be detected by transmittance technique due to the strong absorption (Fig. 1).^{9–11} The reliability of the inverse synthesis method mainly depends on the validity of the optical model and the fitting statistics. Therefore, one can take advantages of solid state spectroscopy to further study the promising ternary system. In the Letter, we estimated the interband critical point energies of PIN-PMN-PT crystals by combining spectral transmittance with reflectance located in the ultraviolet energy range. Effects from temperature and PT concentration on electronic band structure have been discussed in detail.

PIN-PMN-PT single crystals were grown using a vertical Bridgman technique.¹² The samples were cut perpendicular to the $\langle 001 \rangle$ direction. The nominal concentration of $x\text{PIN}\text{-(}1-x-y\text{)PMN}\text{-}y\text{PT}$ crystals was $x \sim 0.27\text{--}0.28$ and $y \sim 0.29\text{--}0.35$. All PIN-PMN-PT crystals were double-side polished with a mechanical polishing process to smooth the

^{a)}Author to whom correspondence should be addressed. Electronic mail: zghu@ee.ecnu.edu.cn. Tel.: +86-21-54345150. Fax: +86-21-54345119.

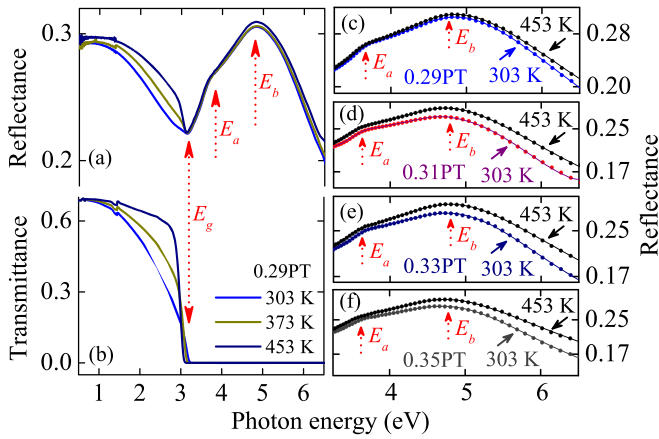


FIG. 1. (a) Reflectance and (b) transmittance spectra of PIN-PMN-0.29PT crystal at the temperatures of 303 K, 373 K, and 453 K, respectively. The experimental (dots) and calculated (solid lines) reflectance spectra of (c) PIN-PMN-0.29PT, (d) PIN-PMN-0.31PT, (e) PIN-PMN-0.33PT, and (f) PIN-PMN-0.35PT crystals at 303 K and 453 K, respectively. The arrows indicate the corresponding interband transitions.

surface. Then the crystals were rigorously cleaned in pure ethanol with an ultrasonic bath and rinsed several times by deionized water for spectral measurements. The surface morphology of the crystals was examined by atomic force microscopy (AFM: Digital Instruments Icon, Bruker). The normal-incident transmittance spectra and near-normal incident (about 8°) reflectance spectra were measured by a double beam ultraviolet-infrared spectrophotometer (PerkinElmer UV/VIS Lambda 950) at the wavelength range of 2650–190 nm (0.5–6.5 eV) with a spectral resolution of 2 nm. The samples were mounted on a heating stage (Bruker A511), which can be varied from RT to 453 K with a step of ± 1 K.

Figs. 1(a) and 1(b) show reflectance and transmittance spectra of PIN-PMN-0.29PT single crystal from near infrared to ultraviolet regions at different temperatures, respectively. With increasing photon energy, the transmission decreases quickly and falls down to zero at about 3.18 eV, indicating an optical absorption edge. This process excites an electron from the filled valence band to an elevated state of the conduction band. The primary contribution of optical loss is from the bandgap and domain wall scattering, which becomes increasingly crucial for photon energies near the bandgap. Lattice dynamical theories indicate that optical properties as well as static dielectric behavior are mainly determined by the BO_6 octahedra because the B-site cation d orbitals and the O-anion $2p$ orbitals associated with each octahedron contribute to the lower conduction bands and the

upper valence bands.¹³ Electronic band structures of ABO_3 perovskite are closely relative to the BO_6 octahedron and sensitive to the B-site atom concentration. The B-site ion plays more important role in the refined energy level as compared to the A-site. For PIN-PMN-PT crystals, Mg^{2+} , Nb^{5+} , In^{3+} , Ti^{4+} ions occupy the octahedral B site disorderedly, giving rise to the disorder and the random fields. The substitution of Ti^{4+} for the complex $(\text{In}_{1/2}\text{Nb}_{1/2})^{4+}$ and $(\text{Mg}_{1/3}\text{Nb}_{2/3})^{4+}$ ions prefers the development of macro-polar domains from nanopolar regions inherently present in relaxors. The nanoregions, domain structure, and order/disorder state of the B-site cation structure have strong effects on the dielectric functions of the crystal.

The main spectral features in Figs. 1(a) and 1(b) are centered at 3.18 ± 0.02 , 3.62 ± 0.07 , and 4.75 ± 0.02 eV, which are labeled as E_g , E_a , and E_b , respectively. These features have been also reported in ferroelectrics PbTiO_3 PT, PbZrO_3 (PZ), PZT, $(1-x)\text{Pb}(\text{Sc}_{1/2}\text{Ta}_{1/2})\text{O}_3$ - $x\text{PbHfO}_3$ (PSTH), and $\text{Pb}(\text{ZrSnTi})\text{O}_3$ (PZST).^{14–17} The structures shift to a lower energy side and become broader with increasing temperature. According to the experimental data as well as local density approximation electronic band structure calculations, the critical point energies for PT at 3.78, 4.00, and 4.93 eV are attributed to $X_{5'v} - X_{3c}$ transition, $X_{4'v} - X_{3c}$ transition, and $X_{5'v} - X_{1c}$ transition, respectively.^{16,17} An anticrossing of critical point energies for PZT occurred, which is due to the coupling between X_{1c} and X_{3c} bands, arising from intrinsic alloy disorder. The potential fluctuation caused by alloy disorder induces a coupling between the degenerate bands.¹⁶ Figs. 1(c)–1(f) show reflectance spectra of PIN-PMN-PT crystals at 303 K and 453 K, respectively. Two obvious peak positions E_a and E_b are located at 3.62 eV and 4.75 eV for PIN-PMN-0.29PT crystal, which are consistent with the fitted peak position energies E_{p1} (3.61 ± 0.07 eV) and E_{p2} (4.74 ± 0.02 eV), as shown in Table I.

Fig. 2(a) shows that the most obvious temperature effect on the transmittance spectra is from the visible region, which is close to the onset of electronic density of states (DOS) at the conduction band. The first principle study reveals that the conduction bands of PMN are primarily from niobium (Nb) $4d$ near the bandgap and become Pb $6p$ at about 5 eV,¹⁸ corresponding to the critical point E_b (4.74 ± 0.02 eV) in the present PIN-PMN-PT system. The electronic DOS at the conduction band edge comes primarily from Nd d states in addition to Pb p and magnesium (Mg)/indium (In) d states. Noticeable Pb p character is distributed through the O p bands while Mg/In d character in the valence bands is not obvious. Considerable Nb d character is concentrated at the

TABLE I. Parameter values of the double Tauc-Lorentz dispersion model for the PIN-PMN-PT crystals are obtained by simulating the near-infrared-ultraviolet reflectance spectra at 303 K (Fig. 1). Note that the unit is eV except for the high-frequency dielectric constant ϵ_∞ , which is dimensionless. The 90% reliability of the fitting parameters is given in parentheses.

xPT	ϵ_∞	TL1				TL2			
		A_1	E_{p1}	Γ_1	E_{t1}	A_2	E_{p2}	Γ_2	E_{t2}
0.29	3.64 (0.03)	120 (35)	3.61 (0.07)	0.89 (0.07)	3.39 (0.03)	139 (7)	4.74 (0.02)	1.91 (0.05)	3.49 (0.04)
0.31	4.22 (0.04)	149 (117)	3.45 (0.21)	0.73 (0.22)	3.45 (0.15)	81 (12)	4.79 (0.04)	1.95 (0.07)	3.28 (0.07)
0.33	3.99 (0.04)	150 (99)	3.46 (0.17)	0.73 (0.17)	3.46 (0.22)	89 (10)	4.81 (0.03)	2.02 (0.05)	3.26 (0.06)
0.35	4.07 (0.08)	154 (142)	3.41 (0.30)	0.86 (0.28)	3.41 (0.25)	91 (21)	4.74 (0.05)	1.93 (0.09)	3.32 (0.11)

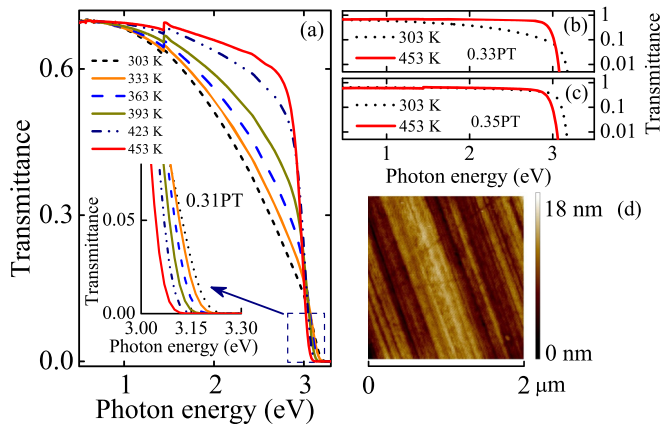


FIG. 2. (a) Transmittance spectra of PIN-PMN-0.31PT crystal at the temperatures of 303 K, 333 K, 363 K, 393 K, 423 K, and 453 K, respectively. The inset shows an enlarged transmittance spectra in the fundamental bandgap region of 3–3.3 eV. Transmittance spectra of (b) PIN-PMN-0.33PT and (c) PIN-PMN-0.35PT crystals at the temperatures of 303 K and 453 K, respectively. Note that the horizontal direction in (b) and (c) is logarithmic coordinate for clarity. (d) AFM surface morphology of PIN-PMN-PT crystals.

bottom of the O p bands, reflecting the main crystal field splitting of the O $2p$ bands into p_{σ} (one per O) and p_{π} (two per O) because of hybridization with Nb. The primary Nb-O hybridization is $e_g - p_{\sigma}$ and Pb p -O p hybridization is not the strongest interaction for the purpose of the O crystal field.¹⁸ The lower valence band for PT consists of two orbitals: one is the Pb $5d$ orbital on the high energy side and the other is the O $2s$ orbital on the low energy. The upper valence band of simple perovskite-type oxides ABO_3 consists of the O $2p$ orbital mixed with the d valence electrons of the B atom.¹⁹ The conduction band consists of the t_{2g} and e_g bands of Ti $3d$ orbital, above which is the Pb $6p$ band. It was reported that the shape of the upper valence band for several Pb-based perovskite-type oxides ABO_3 only changes slightly despite B site substitution while those of the conduction band are remarkably modified by the variation of the B atom.¹⁹ Compared with the electronic structure of PMN, PT, PSTH, and PZST, it is concluded that E_g , E_a , E_b are attributed to transitions from the top of the valence band O $2p$ to the bottom of the conduction band Ti d , Nb d , Pb p , respectively.

The absorption edges of the PIN-PMN-PT crystals show blueshifts trends with decreasing temperature from 453 K to 303 K, as depicted in Fig. 2. Such bandgap narrowing trend with increasing temperature is mainly due to thermal expansion of the lattice and renormalization of electronic band structure by electron-phonon interaction.²⁰ Strain effect originating from the thermal expansion plays an important role in optical properties mainly due to its influence on the orbital overlapping. Note that the bandgap variation trends with increasing temperature for PIN-PMN-0.29PT and PIN-PMN-0.31PT crystals were reported to be widening below RT,⁸ while they become narrowing from 303 K to 453 K. The sudden change of the bandgap trends could be explained by the distinct crystal structures of PIN-PMN-PT solid solutions during the phase transitions with increasing temperature. Lower symmetry monoclinic and/or orthorhombic phases bridge the rhombohedral and tetragonal phases near the

MPB region. Depending on different PT concentrations, they probably coexist with either rhombohedral or tetragonal phase. As a disordered and nonhomogeneous material, the highest structural disorder of PIN-PMN-PT is found near the MPB region, whose phase transitions are from the effect of the correlated ion off-center displacement. Below RT, the coexistence multiphase structure is unstable with increasing temperature due to the stress-relaxation effect. The variation of multiphase content plays a dominant role in the bandgap shrinkage.⁸ However, multiphase structure of PIN-PMN-0.31PT turns to be a rhombohedral phase above RT.²¹ As a result, thermal expansion of the lattice as well as renormalization of the electronic band structure by electron-phonon interaction become the dominant factors for the bandgap narrowing trend with increasing temperature above RT. With increasing temperature, the amplitude of atomic vibrations increases, leading to a larger interatomic spacing. The interaction between the lattice phonons and free electrons influence the bandgap to some extent.

Fig. 2(d) illustrates the AFM surface morphology of PIN-PMN-PT crystals. The root-mean-square (RMS) surface roughness is estimated to be about 2.3 nm. It should be emphasized that surface roughness or scattering effects can be negligible because transmittance and reflectance spectra are recorded at normal-incident and/or near-normal incident (about 8°), respectively. To extract the dielectric function from the reflectance spectra, a physical model expressing the band-band transitions should be applied. The double Tauc-Lorentz (DTL) dispersion model, determined by Tauc joint density of states and the standard quantum mechanical or Lorentz calculation for ϵ_2 (imaginary part of the dielectric function) of a collection of non-interacting atoms,²² is constructed to obtain the dielectric functions of PIN-PMN-PT crystals. The DTL dispersion model can be written as: $\epsilon_1(E) = \epsilon_{\infty} + \frac{2}{\pi} P \int_0^{\infty} \frac{\xi \epsilon_2(\xi)}{\xi^2 - E^2} d\xi$, $\epsilon_2(E) = \sum_{j=1}^2 \frac{A_j E_{pj} \Gamma_j (E - E_{ij})^2}{(E^2 - E_{pj}^2)^2 + \Gamma_j^2 E^2}$ ($E > E_{ij}$). Where ϵ_{∞} is the high-frequency dielectric constant, P is the Cauchy principal part of the integral, E is the incident photon energy, A_j , E_{pj} , Γ_j , and E_{ij} are the amplitude, peak position energy, broadening term, and Tauc gap energy of the j th oscillator, respectively. The above DTL model abides by the Kramers-Kronig transformation in the entirely measured photon energy region, which is applied to semiconductor and dielectric materials.^{14,15,22} At near-normal incidence, the dielectric functions are related to the reflectance R by the Fresnel formula: $R = |(\sqrt{\epsilon(E)} - 1)/(\sqrt{\epsilon(E)} + 1)|^2$. The best-fit parameter values of the model (i.e., dielectric functions) can be obtained as shown in Figs. 1(c)–1(f).

Figs. 3(a) and 3(b) depict the real and imaginary parts of the complex dielectric functions from the DTL dispersion model. Parameter values of the DTL dispersion model are listed in Table I. The optical structures shown in the ϵ spectrum are described by the charge-transfer transitions or the interband transitions.²³ The charge transfer mainly occurs between the Pb $6p$, Ti $3d$, and O $2p$ orbitals during the ferroelectric-paraelectric phase transition. The Pb-O bonding strongly affects O $2p$ -Ti $3d$ hybridization in the TiO_6 octahedron.²⁴ Moreover, all the $\Gamma_1 < \Gamma_2$ shown in Table I indicates that the broadening term of the first oscillator is smaller than that of the second oscillation. To explain the temperature

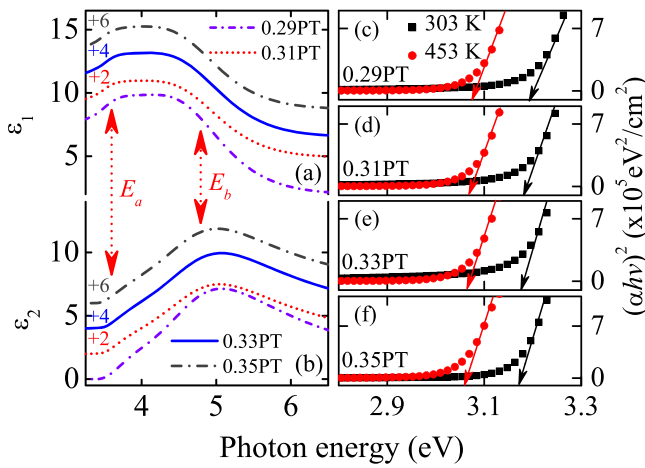


FIG. 3. (a) and (b) Dielectric functions ($\varepsilon = \varepsilon_1 + i\varepsilon_2$) of PIN-PMN-PT crystals at 303 K. The arrows indicate the assignments of electronic band transitions. The variations of $(\alpha hv)^2$ with the photon energy for the (c) PIN-PMN-0.29PT, (d) PIN-PMN-0.31PT, (e) PIN-PMN-0.33PT, and (f) PIN-PMN-0.35PT crystals measured at 303 and 453 K, respectively.

dependent behavior, the OBG energies for PIN-PMN-PT crystals are calculated by considering a direct transition between the valance and conduction bands. Direct transition is a first-order process because no phonon is involved. The absorption coefficient α as a function of photon energy is expressed by the Tauc relation: $\alpha hv \propto (hv - E_g)^{1/2}$, where ν is the frequency, h is the Planck constant, and E_g is the allowed direct OBG energy. Therefore, the straight line between $(\alpha hv)^2$ and hv will provide the OBG value, which is extrapolated by the linear portion of the plot to $(\alpha hv)^2 = 0$, as shown in Figs. 3(c)–3(f). At 303 K, the direct bandgap E_g of PIN-PMN-0.29PT, PIN-PMN-0.31PT, PIN-PMN-0.33PT, and PIN-PMN-0.35PT crystals are 3.18 ± 0.02 , 3.18 ± 0.02 , 3.17 ± 0.02 , and 3.17 ± 0.02 eV, showing a redshift trend with increasing PT concentration. Similar phenomena are also reported in relaxor $\text{PbZn}_{1/3}\text{Nb}_{2/3}\text{O}_3\text{-PbTiO}_3$ (PZN-PT).²⁵ The basic energy levels are determined by the common $(\text{B}_1\text{B}_2)\text{O}_6$ oxygen octahedral structure in $\text{A}(\text{B}_1\text{B}_2)\text{O}_3$ -type perovskite ferroelectrics. Thus, similar optical absorption edges with slight differences are found in PIN-PMN-PT and PZN-PT crystals due to different B-site cations and concentration. Temperature dependence of the critical point energies is displayed in Fig. 4. An empirical formula for the bandgap energy of the relaxor ferroelectric PIN-PMN-PT single crystals versus the temperature (T) and PT concentration (x) can be found as

$$E_g(x, T) = 1.324 + 0.204x - 0.065x^2 + 6.77 \times 10^{-5}x^3 - 8.60 \times 10^{-4}T + 3.41 \times 10^{-6}xT, \quad (1)$$

where $0.29 \leq x \leq 0.35$ and $303 \text{ K} \leq T \leq 453 \text{ K}$ in the present experiment. The fitting lines are well consist with the experimental value, as shown in Figs. 4(c)–4(f).

Deviation from the linear behaviors of critical point energies E_a and E_b as a function of PT concentration is observed from Figs. 4(a) and 4(b) with different structures labeled. Note that the structures of the present PIN-PMN-PT crystals are different according to the x-ray diffraction.^{8,21} Such deviation from the linear behavior indicates an effect of phase transitions on the critical point energies. The ABO_3

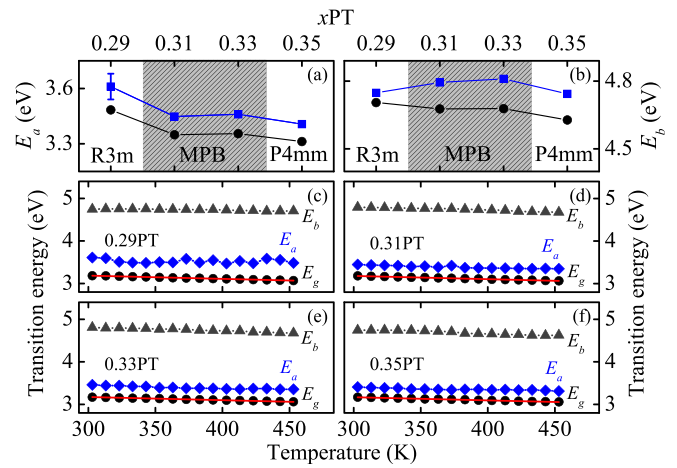


FIG. 4. The critical point energies (a) E_a and (b) E_b as a function of the PT concentration for the PIN-PMN-PT crystals. A representative error bar is shown. Note that the shade parts approximately correspond to the MPB region. Temperature dependence of the critical point energies for (c) PIN-PMN-0.29PT, (d) PIN-PMN-0.31PT, (e) PIN-PMN-0.33PT, and (f) PIN-PMN-0.35PT crystals, respectively. Note that the dotted and solid lines in (c)–(f) indicate the experimental determination and fitting data by the empirical formula, respectively.

perovskite structure is a three-dimensional network of regular corner-linked BO_6 , octahedra with B cations at the center of each octahedron and A cations being centrally located in the AO_{12} cuboctahedral cavity formed by eight octahedra. The tetragonal and rhombohedral phases might coexist and various low-symmetry phases have been postulated in the MPB region, indicating a complicated chemical structure of PMN-PT based solid solutions.²⁶ Synchrotron x-ray powder diffraction measurements reveal that the orthorhombic or monoclinic phase of M_C type with space group Pm coexist with either rhombohedral or tetragonal phase in the MPB and their volume fractions changes with increasing temperature.²⁷ Temperature dependent dielectric constant, piezoelectric resonance frequency and powder neutron diffraction studies suggest a M_B type with space group Cm existing in PT poor region of MPB. The short range M_B type monoclinic order at RT can grow to long range monoclinic order on lowering the temperature.²⁸ Moreover, three intermediate phases including one orthorhombic phase and two monoclinic phases are proposed to separate the tetragonal and rhombohedral phase.²⁹ Such low symmetry phases were even observed in a wide PT concentration range of 0.3–0.47.³⁰ The phase transition between two monoclinic phases is of first order and shows a large thermal hysteresis.³¹ A similar competing mechanism between rhombohedral and monoclinic order is reported in PZT crystal near MPB region as well.³² The complex MPB states of the PMN-PT/PIN-PMN-PT systems point to an energy balance between different phases, which is much more delicate than that of PZT based system.

In conclusion, we have investigated optical properties and electronic band structures of (001)-face PMN-PT single crystals around MPB region by transmittance and reflectance spectra from 303 to 453 K. Three typical interband transitions and dielectric functions are correlated with structural changes from rhombohedral to tetragonal phase. Deviation from the linear behaviors of critical point energies E_a and E_b

versus PT concentration can be observed, indicating that the variation of electronic band structures are closely related to the phase transitions.

This work was financially supported by Major State Basic Research Development Program of China (Grant Nos. 2011CB922200 and 2013CB922300), Natural Science Foundation of China (Grant Nos. 11374097 and 61376129), Projects of Science and Technology Commission of Shanghai Municipality (Grant Nos. 13JC1402100 and 13JC1404200), and the Program for Professor of Special Appointment (Eastern Scholar) at Shanghai Institutions of Higher Learning.

- ¹L. E. Cross, *Ferroelectrics* **76**, 241 (1987).
- ²H. Fu and R. E. Cohen, *Nature (London)* **403**, 281 (2000).
- ³H. You and Q. M. Zhang, *Phys. Rev. Lett.* **79**, 3950 (1997).
- ⁴W. Zhong and D. Vanderbilt, *Phys. Rev. Lett.* **74**, 2587 (1995).
- ⁵S. E. Park and T. R. Shrout, *J. Appl. Phys.* **82**, 1804 (1997).
- ⁶Z. G. Ye, *MRS Bull.* **34**, 277 (2009).
- ⁷G. Burns and B. A. Scott, *Solid State Commun.* **13**, 423 (1973).
- ⁸J. J. Zhu, W. W. Li, G. S. Xu, K. Jiang, Z. G. Hu, and J. H. Chu, *Acta Mater.* **59**, 6684 (2011).
- ⁹K. Y. Chan, W. S. Tang, C. L. Mak, and K. H. Wong, *Phys. Rev. B* **69**, 144111 (2004).
- ¹⁰X. L. Zhang, Z. G. Hu, G. S. Xu, J. J. Zhu, Y. W. Li, Z. Q. Zhu, and J. H. Chu, *Appl. Phys. Lett.* **103**, 051902 (2013).
- ¹¹J. J. Zhu, W. W. Li, G. S. Xu, K. Jiang, Z. G. Hu, M. Zhu, and J. H. Chu, *Appl. Phys. Lett.* **98**, 091913 (2011).
- ¹²G. S. Xu, K. Chen, D. F. Yang, and J. B. Li, *Appl. Phys. Lett.* **90**, 032901 (2007).
- ¹³M. DiDomenico, Jr. and S. H. Wemple, *J. Appl. Phys.* **40**, 720 (1969).
- ¹⁴W. J. Zhang, Z. H. Duan, K. Jiang, Z. G. Hu, G. S. Wang, X. L. Dong, and J. H. Chu, *Acta Mater.* **60**, 6175 (2012).
- ¹⁵X. Chen, K. Jiang, Z. G. Hu, X. F. Chen, G. S. Wang, X. L. Dong, and J. H. Chu, *Appl. Phys. Lett.* **101**, 011914 (2012).
- ¹⁶T. D. Kang, H. Lee, G. Xing, N. Izumskaya, V. Avrutin, B. Xiao, and H. Morkoç, *Appl. Phys. Lett.* **91**, 022918 (2007).
- ¹⁷J. Robertson, W. L. Warren, and B. A. Tuttle, *J. Appl. Phys.* **77**, 3975 (1995).
- ¹⁸M. Siewattana and D. J. Singh, *Phys. Rev. B* **73**, 224105 (2006).
- ¹⁹M. Kitamura and H. Chen, *Ferroelectrics* **210**, 13 (1998).
- ²⁰H. Y. Fan, *Phys. Rev.* **82**, 900 (1951).
- ²¹J. J. Zhu, K. Jiang, G. S. Xu, Z. G. Hu, Y. W. Li, Z. Q. Zhu, and J. H. Chu, *J. Appl. Phys.* **114**, 153508 (2013).
- ²²G. E. Jellison, Jr. and F. A. Modine, *Appl. Phys. Lett.* **69**, 371 (1996); **69**, 2137 (1996).
- ²³S. G. Choi, H. T. Yi, S. W. Cheong, J. N. Hifiker, R. France, and A. G. Norman, *Phys. Rev. B* **83**, 100101(R) (2011).
- ²⁴J. C. Jan, H. M. Tsai, C. W. Pao, J. W. Chiou, K. Asokan, K. P. K. Kumar, W. F. Pong, Y. H. Tang, M. H. Tsai, S. Y. Kuo, and W. F. Hsieh, *Appl. Phys. Lett.* **87**, 012103 (2005).
- ²⁵E. Sun, R. Zhang, Z. Wang, D. Xu, L. Li, and W. Cao, *J. Appl. Phys.* **107**, 113532 (2010).
- ²⁶R. A. Cowley, S. N. Gvasaliya, S. G. Lushnikov, B. Roessli, and G. M. Rotaru, *Adv. Phys.* **60**, 229 (2011).
- ²⁷B. Noheda, D. E. Cox, G. Shirane, J. Gao, and Z. G. Ye, *Phys. Rev. B* **66**, 054104 (2002).
- ²⁸A. K. Singh, D. Pandey, and O. Zaharko, *Phys. Rev. B* **74**, 024101 (2006).
- ²⁹Z. Kutnjak, J. Petzelt, and R. Blinc, *Nature* **441**, 956 (2006).
- ³⁰V. A. Shuvaeva, A. M. Glazer, and D. Zekria, *J. Phys.: Condens. Matter* **17**, 5709 (2005).
- ³¹D. Zekria, V. A. Shuvaeva, and A. M. Glazer, *J. Phys.: Condens. Matter* **17**, 1593 (2005).
- ³²D. Phelan, X. Long, Y. Xie, Z. G. Ye, A. M. Glazer, H. Yokota, P. A. Thomas, and P. M. Gehring, *Phys. Rev. Lett.* **105**, 207601 (2010).